Ceramics-Silikáty 70 (1), 1-11 (2026)
www.ceramics-silikaty.cz doi: 10.13168/cs.2025.0046

INFLUENCE OF CHLORIDE SALTS ON THE CHLORIDE BINDING CAPACITY OF AN ALKALI-ACTIVATED SLAG

GAOFENG ZHOU*, **, #WEI CHEN*, DAZHI WU**, KEYU CHEN***, PEIJUN TIAN****, MEILING CHEN**

*School of Civil Engineering and Architecture, NingboTech University, Ningbo, 315100, PR China
**School of Civil Engineering and Architecture, Zhejiang Sci-Tech University, Hangzhou, 300018, PR China
***School of Civil Engineering and Architecture, Zhejiang University, Hangzhou 310058, PR China
****Ningbo Dongxing Asphalt Products Co Ltd, Ningbo, 315100, PR China

#E-mail: chenw@nbt.edu.cn, 906843804@qq.com

Submitted June 10, 2025; accepted September 19, 2025

Keywords: Alkali-activated slag, Chloride binding capacity, Chloride binding isotherm, Chloride salt type, Friedel's salt

Chloride binding is a key factor affecting chloride-induced corrosion in reinforced concrete. Different types of chloride salts may exhibit distinct binding mechanisms. In this work, the influence of chloride salts (NaCl, $MgCl_2$, and $CaCl_2$) on the chloride ion binding mechanism in alkali-activated slag (AAS) was investigated. The pH value, chloride ion binding capacity, and phase evolution of AAS were examined through various experimental and analytical methods. To compare the phase compositions of AAS after chemical equilibrium under exposure to different chloride solutions, thermodynamic modelling was employed to predict the phase assemblages in AAS. The study revealed that the type of chloride salt significantly influences the chloride-binding capacity and pore solution pH of AAS. The binding capacity followed the order: $CaCl_2$ > $MgCl_2$ > NaCl. Compared to $CaCl_2$ and $MgCl_2$, exposure to the NaCl solution increased the pore solution pH of AAS, thereby reducing the solubility of Friedel's salt and MgAl-LDHs (layered double hydroxides) and releasing more bound chloride ions. The X-ray diffraction (XRD) and thermogravimetric analysis (TGA) results demonstrated that AAS exposed to the $CaCl_2$ solution exhibited the enhanced formation of C-A-S-H, which contributed to the higher physical adsorption of chloride ions. In the $MgCl_2$ solution, magnesium plays a dual role: it reacts with C-A-S-H phases, leading to a reduction in the pore solution pH; it provides favourable conditions for the precipitation of MgAl-LDHs, thereby enhancing the chloride ion binding. Furthermore, within the water-to-binder ratio range of 0.35 – 0.45, increasing the ratio enhances the chloride-binding capacity of AAS, but has negligible effects on the pH of the pore solution.

INTRODUCTION

The concrete infrastructure, particularly reinforced concrete structures in coastal areas, often experiences premature failure due to inadequate durability design considerations. This is primarily attributed to the high susceptibility of reinforced concrete to chloride-induced corrosion damage [1-4]. Specifically, when steel reinforcement is exposed to seawater containing high chloride concentrations, the chloride ions typically disrupt the passive film on the steel surface, subsequently initiating electrochemical corrosion of the reinforcement [3, 5]. At the forefront of chloride-induced corrosion durability research, it is widely accepted that free chloride ions are the primary culprits responsible for the steel reinforcement corrosion damage [6, 7], while bound chloride ions exhibit significantly less detrimental effects on the reinforcement [8]. Bound chloride ions exist primarily through two mechanisms: physical adsorption onto the surface of cementitious hydration products via electrostatic attraction and van der Waals forces, and chemical binding within the hydration products through reactions forming stable phases such as Kuzel's salts, Friedel's salt, and MgAl-LDHs [9, 10]. However, bound chloride ions tend to exhibit varying stability under different environmental conditions, such as acidification, elevated temperatures, and exposure to different types of chloride salt cations [11-13]. When bound chloride ions in concrete become destabilised, they can transform into free chloride ions, which can adversely affect the durability of reinforced concrete structures. Consequently, the impact of bound chloride ions on structural durability must not be overlooked.

Ordinary Portland cement (OPC) remains the most widely used construction material in practical engineering applications. However, due to its substantial greenhouse gas emissions during production, the pursuit of low-carbon alternative cementitious materials has become increasingly attractive [14]. AAS is synthesized by mixing granulated blast furnace slag (GGBS) with alkaline solutions. Compared to OPC, AAS demonstrates significantly lower carbon emissions while exhibiting comparable or even superior mechanical properties [15, 16]. Furthermore, studies have revealed that clinker-free AAS exhibits superior performance in terms of abrasion resistance [17], sulfate attack mitigation [18], and embedded steel corrosion protection [19]. Consequently, AAS has garnered significant attention as a high-performance alternative to OPC. However, AAS currently faces several critical challenges. For instance, it is prone to shrinkage cracking and alkali-silica reaction (ASR) [20-23]. Moreover, one of the most significant barriers to its practical application remains the uncertain durability performance in chloride-laden environments.

In practical engineering applications, steel corrosion in concrete is rarely induced by a single chloride salt type. For instance, de-icing salts (used for snow melting) and seawater contain complex chloride compositions - while NaCl is predominant, significant concentrations of $CaCl_2$ and $MgCl_2$ are also present [24]. In OPC systems, the physicochemical environment within concrete varies significantly depending on the type of chloride salts present. Research has reported that the presence of $CaCl_2$ inhibits the $Ca(OH)_2$ precipitation and reduces the pore solution pH in concrete, whereas NaCl tends to increase the pH of the concrete pore solution [25]. At equivalent concentrations, $CaCl_2$ solutions exhibit a higher chloride-binding capacity with hydration products and a lower free chloride ion content in pore solutions compared to NaCl systems. In terms of steel reinforcement corrosion, Zhu's study found that compared to NaCl and KCl solutions, exposure to a $CaCl_2$ solution significantly increased the corrosion rate of the rebar in OPC by generating a greater amount of $Ca(OH)_2$ [26]. In addition to the varying corrosion rates of the steel reinforcement, the incorporation of different types of chlorides can also lead to changes in the pore structure of concrete. It is reported that $CaCl_2$-doped concrete develops a more porous and less dense matrix compared to NaCl-doped systems, directly compromising its mechanical strength [27]. In contrast to OPC, AAS possesses distinct gel structures and hydration products. Specifically, the primary gel phase in AAS-C-A-S-H contains an elevated aluminium content, which may fundamentally alter the adsorption mechanisms for different chloride salt cations (e.g., Na^+, Ca^{2+}, Mg^{2+}). Furthermore, AAS hydration generates not only AFm-type phases but also MgAl-LDHs. Studies demonstrate that MgAl-LDHs effectively reduce the free anion concentrations in pore solutions through interlayer ion exchange and surface charge-balancing adsorption mechanisms [28]. This unique capability is considered a primary factor endowing AAS with the enhanced chloride-binding capacity relative to conventional OPC systems [29]. However, the observed effects of different types of chlorides on the binding of hydrotalcite and AFm may vary accordingly. Moreover, some studies have found that under unstable conditions, the acid-neutralising capacity of Friedel's salts is enhanced, but no significant changes were observed in the NaCl solution [27]. Based on the above, the type of chloride ions has a significant impact on the corrosion of steel reinforcement, chloride ion binding, and both macro- and micro-structural properties of cement-based materials. However, the current research on the influence of chloride cation types on the chloride ion binding in cement-based materials mainly focuses on OPC systems, with no studies linking it to AAS. Considering the differences in the microstructure and hydration products between AAS and OPC, these differences may result in variations in the adsorption mechanisms of different types of chloride ions. Therefore, studying the impact of different chloride salts on the chloride ion binding mechanisms in AAS is of significant importance.

In summary, the primary objective of this study is to investigate the effects of three cation types (Mg^{2+}, Ca^{2+}, and Na^+) on the chloride-binding mechanisms in AAS systems. This study employs X-ray diffraction (XRD) and Thermogravimetric- Derivative Thermogravimetry (TG-DTG) analyses to examine the mineralogical evolution of AAS and its chloride-induced alterations, thereby elucidating upon the reaction mechanisms between AAS and the different chloride salts (NaCl, $CaCl_2$, $MgCl_2$). These techniques aim to reveal the underlying mechanisms governing the distinct behaviours of bound chloride ions under varying salt conditions. Thermodynamic modelling was incorporated to establish correlations between the experimental results and simulated phase assemblages, with the expectation that such a comparative analysis would yield novel insights into the chloride-binding mechanisms in AAS. These findings are anticipated to advance the theoretical frameworks for understanding both the chloride-binding capacity of AAS and strategies for enhancing the durability of marine structures exposed to chloride-laden environments.

EXPERIMENTAL

Materials

In this study, the precursors, GGBS, used in this study were supplied by Henan Yuanheng Environmental Protection Engineering Co., Ltd. The alkali activator was prepared by dissolving flake sodium hydroxide (analytical grade) in a sodium silicate solution (50° Bé, original modulus of 3.3) to achieve a final activator modulus of 1.5. The oxide composition and mineralogical characteristics of the raw materials, as determined by X-ray fluorescence (XRF) spectroscopy and XRD analysis, are presented in Table 1 and Figure 1, respectively. The particle size distribution, as measured by laser diffraction analysis using a Malvern Mastersizer 3000 instrument, is presented in Figure 2. Given the varying salt concentrations in de-icing agents and seawater—where NaCl, $MgCl_2$, and $CaCl_2$ serve

Table 1. Oxide composition of raw materials determined by XRF (wt. %).

	SiO_2	Al_2O_3	CaO	MgO	Fe_2O_3	Na_2O	K_2O	TiO_2	LOI
GGBS	31.58	15.28	43.17	6.67	0.23	0.21	0.45	0.74	1.67

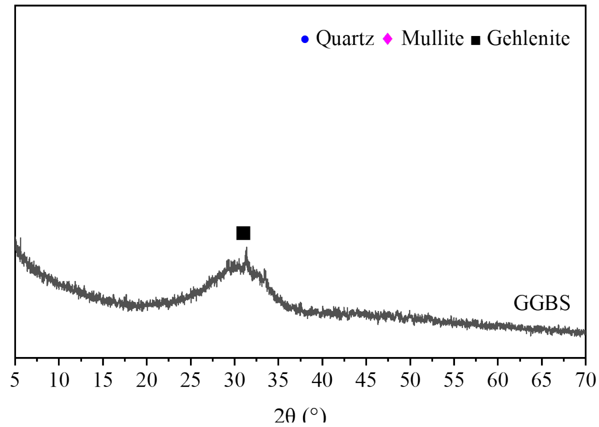

Figure 1. XRD patterns of the precursors.

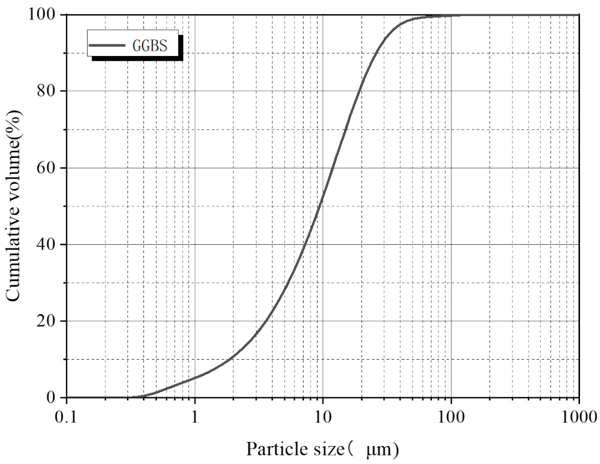

Figure 2. Particle size distribution of the precursors.

as the primary chloride constituents - this study employed solutions of these three salts at different concentrations as the exposure media.

Sample preparation

The AAS cement paste specimens were prepared according to the mix proportions detailed in Table 2. The specimen preparation procedure strictly followed the Chinese national standard GB/T 1346-2011 [30]. The slag was introduced into the mixer bowl containing the activator solution. The paste was first mixed at a low speed for 30 seconds, followed by a 15-second pause during which the paste adhering to the bowl's sides was scraped down. Subsequently, mixing resumed at a medium speed for 60 seconds to ensure homogeneity. Following the thorough mixing, the paste was cast into 40 × 40 × 40 mm cubic moulds. After 24 hours of curing, the specimens were demoulded and subsequently transferred to a constant-temperature water bath maintained at 20 °C. This protocol was specifically designed to optimise the hydration development while simultaneously minimising the carbonation-induced degradation of the specimens. According to the Chinese national standard GB/T 17671-2021[31], the 28-day unconfined compressive strength test was conducted on the specimens, and the 28-day strength is shown in Table 2.

Chloride binding isotherm

The experiments were conducted using the adsorption isotherm equilibrium method developed by Tang et al. [32]. The specific experimental procedures are shown in Figure 3. To obtain sufficiently fine powder samples, the 28-day cured specimens were crushed and then dried in a vacuum oven at 60 °C for a minimum of 72 hours. The dried samples were further ground to pass through a 100-mesh sieve and stored in sealed bags to prevent moisture absorption.

The collected powder samples (5 g aliquots) were dispersed into 50 mL centrifuge tubes, followed by the addition of 40 mL of an exposure solution using a volumetric pipette. The exposure solutions were prepared using analytical-grade chloride salts (NaCl, $CaCl_2$, and $MgCl_2$) at concentrations of 0.2, 0.6, 1, and 2 M. The sealed centrifuge tubes were maintained at 23.0 ± 2.0 °C and periodically agitated to ensure thorough solid-liquid interaction. Typically, a 14-day equilibrium period was adopted to ensure complete

Table 2. Mixing parameters of the blended AAS pastes (in wt. %).

MIX ID	Slag (wt. %)	Activator Na_2SiO_3	Activator NaOH	W/C mass ratio	Na_2O (wt. %)	Strength (MPa) 28 d
S35	100	19.48	1.843	0.35	4	82.1
S40	100	19.48	1.843	0.4	4	85.4
S45	100	19.48	1.843	0.45	4	88.3

equilibration between the pore solution in the powder samples and the host solution, based on empirically validated durations from prior studies. To guarantee a complete solid-liquid interaction, the samples in this study were stored for one month prior to analysis [33, 34]. After one month of storage, the centrifuge tubes were subjected to centrifugation at 3500 rpm for 5 minutes. The supernatant was then extracted through a fibre bundle filter (4 μm pore size), with 3 mL aliquots transferred to 5 mL plastic tubes for the subsequent chloride ion concentration (C_1) analysis using potentiometric titration (ZDJ-4A). The remaining supernatant was similarly filtered through a 4 μm fibre bundle filter and aliquoted into 15 mL plastic tubes for the subsequent pH measurement. Following extraction, solid-liquid separation was performed using a Büchner funnel under vacuum filtration. The solids were then sequentially rinsed with distilled water (once) and isopropanol (twice) to remove the loosely bound chloride ions. The particles were then vacuum-dried at 45 °C, subsequently ground to pass through a 200--mesh sieve, and prepared for further analysis.

For the determination of the bound chloride ions, it was postulated that the observed concentration change in the chloride solution after achieving solid-liquid equilibrium resulted exclusively from the chloride ion binding. The quantity of bound chloride ions was calculated using Equation (1). The experimentally determined chloride binding data were fitted to the Langmuir isotherm model, as represented by Equation (2).

$$C_b = \frac{35.45V\ (C_0 - C_1)}{G} \tag{1}$$

$$C_f = \frac{\alpha C_f}{1 + \beta C_f} \tag{2}$$

C_b represents the total bound chloride content per unit mass of the powdered sample (mg·g^{-1}); V denotes the initial volume of the chloride solution (ml); C_0 presents the initial chloride concentration of the immersion solution (mol·L^{-1}); C_1 corresponds to the equilibrium chloride concentration (mol·L^{-1}); G designates the initial mass of the sample in the chloride solution (g) and α and β are the binding constants.

pH test

The pH of the extracted supernatant samples was measured using an Orion Star A3250 instrument (Thermo Fisher Scientific). Prior to testing, the electrode was calibrated using buffer solutions at pH 7, 10, and 13. The calibrated electrode was then fully immersed in the 15 mL extracted solution for the measurement. Following each measurement, the electrode was

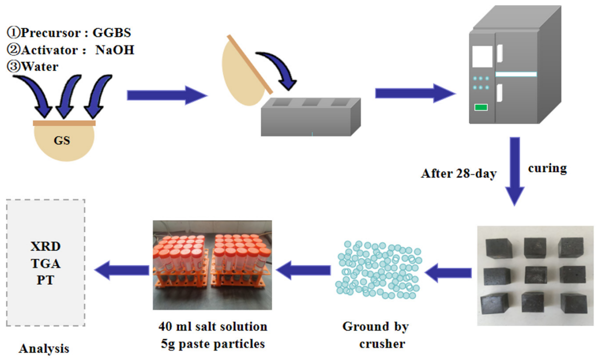

Figure 3. The flowchart for the preparation of samples for investigations.

thoroughly rinsed with deionised water and dried with lint-free wipes. Triplicate pH measurements were performed for every sample to ensure data reproducibility.

XRD analysis

The mineralogical evolution of the AAS powders exposed to chloride solutions was investigated using XRD. The crystalline phases of the samples were analysed using XRD patterns collected by a Rigaku Ultima IV diffractometer (Japan) with Cu-Kα radiation (λ = 1.541 Å). The XRD analysis was conducted at 40 mA current and 40 kV voltage, with a scanning range of 5° to 70° 2θ and a step size of 0.033° 2θ.

TGA analysis

TGA was performed using a NETZSCH STA 449 F5 Jupiter instrument under a nitrogen atmosphere (20 mL·min^{-1} flow rate). Approximately 50 mg of the AAS powder was loaded into a ceramic crucible and heated from 30 to 900 °C, with the continuous recording of the mass loss and its derivative (DTG) across the temperature range.

Thermodynamic model

The thermodynamic modelling of AAS was conducted using GEMS 3.5 (Gibbs Energy Minimization Software [35]), establishing a predictive phase evolution model under different chloride solutions. The primary reaction products in AAS were described using a solid solution model for the C-(N)-A-S-H and Mg-Al LDH phases [36]. NaCl was employed as the background electrolyte, with the mean ionic diameter set to 3.72 Å, short-range interaction parameter at 0.064 kg·mol^{-1}, and activity coefficients of neutral dissolved species fixed at unity. During the thermodynamic calculations, the raw material composition was input as oxide percentages (determined by X-ray fluorescence (XRF)). Given the lack of reliable thermodynamic data for Fe_2O_3 and TiO_2 in the reaction system, these oxides were excluded from the simulations and assumed not to form any relevant phases. Experimental studies by Myers et al. [36, 37] demonstrated that AAS cement achieves a reaction degree of 54 ± 3 % after 30 days of curing, with minimal subsequent increase. Based on these findings, the slag reaction degree was conservatively to be 60 % for modelling purposes.

RESULTS AND DISCUSSION

The influence of the cation types on the chlorine binding capacity of AAS

Table 3 presents the Langmuir isotherm fitting para-meters for the AAS samples prepared with three distinct water-to-binder ratios (0.35, 0.40, and 0.45). Figure 4 illustrates the correlation between the free and bound chloride ions in the AAS following exposure to the three different chloride solutions. As evident from the Figure 4, the chloride binding isotherm of AAS shows excellent agreement with the Langmuir isotherm model. The increase in the water-to-binder ratio demonstrates a positive correlation with the chloride-binding capacity of AAS, consistent with established findings in prior research [26]. Furthermore, exposure to all three chloride salts revealed a consistent trend: the chloride-binding capacity of each specimen increased progressively with the higher chloride concentrations. This phenomenon primarily stems from the enhanced chloride binding capacity at elevated concentrations, where the increased collision frequency between the chloride ions and hydration products (e.g., C-(N)-A-S-H, LDHs) promotes both chemical incorporation and physical adsorption mechanisms. More specifically, the increased chloride concentration enhances the interaction probability between the free chloride ions and gel phases (e.g., C-(N)-A-S-H, LDHs), thereby facilitating greater chloride adsorption through combined the van der Waals attraction and electrostatic charge-balancing mechanisms [12]. The experimental data demonstrate that the chloride-binding capacity of AAS is significantly influenced by the type of chloride salt, exhibiting the following overall trend: $CaCl_2$ > $MgCl_2$ > NaCl. Compared to Na^+ systems, AAS exposed

Table 3. The fitting parameters of the Langmuir isotherms.

W/C	Mix ID	α	β	R^2
	NaCl	22.02	0.94	0.992
0.35	$MgCl_2$	38.24	1.46	0.975
	$CaCl_2$	42.63	1.25	0.962
	NaCl	20.23	0.71	0.984
0.40	$MgCl_2$	31.44	0.92	0.964
	$CaCl_2$	38.33	0.87	0.975
	NaCl	21.17	0.65	0.980
0.45	$MgCl_2$	29.97	0.78	0.972
	$CaCl_2$	37.70	0.76	0.961

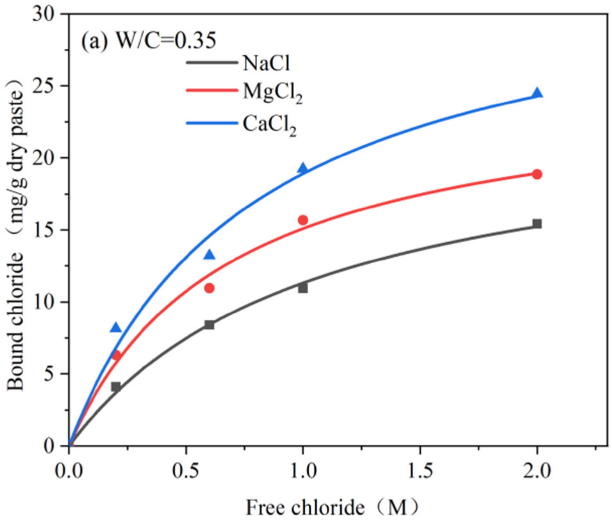

a) W/C = 0.35

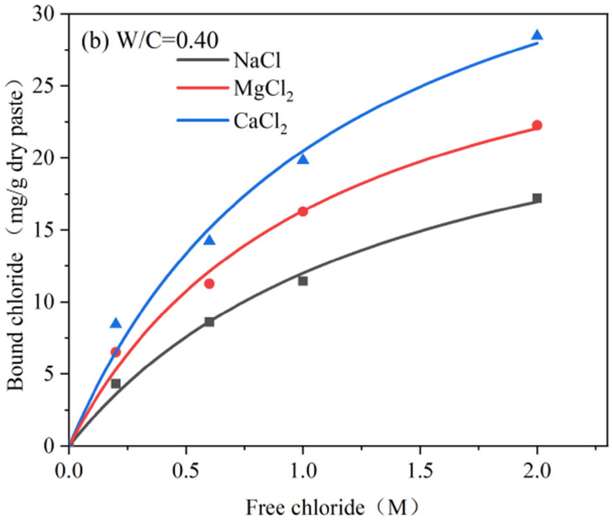

b) W/C = 0.40

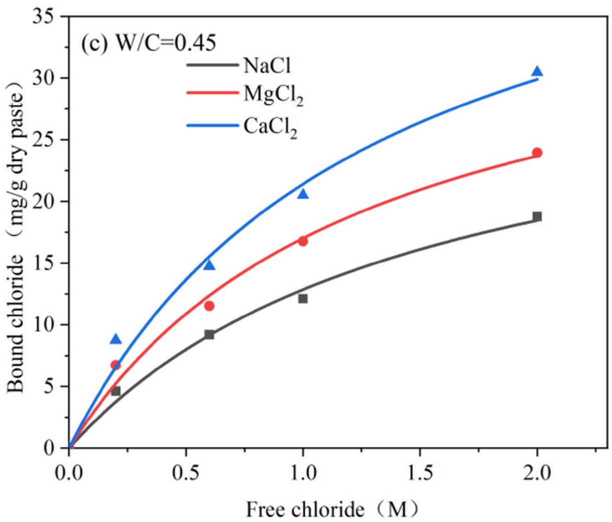

c) W/C = 0.45

Figure 4. The chloride ion binding isotherm of the AAS pastes after exposure to the chloride solution.

to Ca^{2+} and Mg^{2+} solutions exhibited approximately 60 and 30 % higher chloride-binding capacities, respectively, at the 2 M exposure level. The underlying mechanisms governing these differential binding behaviours will be systematically analysed in the subsequent sections.

The change of pH in the supernatant

Figure 5 presents the pH values of the supernatant solutions under three distinct water-to-binder ratios (0.35, 0.40, and 0.45). The data reveal a consistent pH trend across all the systems: NaCl-exposed AAS > $CaCl_2$-exposed AAS > $MgCl_2$-exposed AAS. The increase in the water-to-binder ratio induced a moderate elevation in the supernatant pH, likely due to the enhanced hydration degree of AAS at higher water contents. The NaCl-exposed systems exhibited the highest supernatant pH values, with a slight, but consistent increase in the pH observed at elevated chloride concentrations. This trend aligns with the established literature findings [26]. In contrast, the $MgCl_2$-exposed systems displayed significant pH fluctuations. At a 0.2 M exposure concentration (w/b = 0.4), the pH measured 11.72, whereas a > 30 % pH reduction occurred when the concentration reached 2 M. This phenomenon is likely attributed to the reaction between Mg^{2+} from the $MgCl_2$ solution and hydroxyl groups, resulting in the precipitation of a small amount of $Mg(OH)_2$ and the consequent consumption of hydroxyl ions in the solution. Furthermore, studies have revealed that elevated Mg^{2+} concentrations in pore solutions can promote the transformation of gel phases into M-A-S-H [38], consequently altering the pore solution pH. Similar to $MgCl_2$, the $CaCl_2$-exposed solutions exhibited a concentration-dependent decrease in the supernatant pH. This phenomenon may be attributed to the reaction between the free calcium ions (Ca^{2+}) in the pore solution and dissolved slag constituents, leading to the enhanced formation of the calcium-containing phases (e.g., C-A-S-H, Friedel's salt). This process consumes hydroxyl ions (OH^-), thereby reducing the solution pH [39].

XRD analysis

Figure 6 presents the XRD patterns of AAS (w/b = 0.4) after 28 days of immersion in the three chloride solutions. The XRD patterns reveal detectable calcite peaks, demonstrating both thorough solid-liquid reactions and minimal carbonation interference in the experimental system. Friedel's salt was identified in all three chloride solutions, confirming the chemical binding between chloride ions and the AAS products. In the NaCl-exposed systems, MgAl-LDHs, C-A-S-H, and Friedel's salt were consistently identified, aligning with established findings in prior studies [40]. The XRD patterns show enhanced diffraction peaks

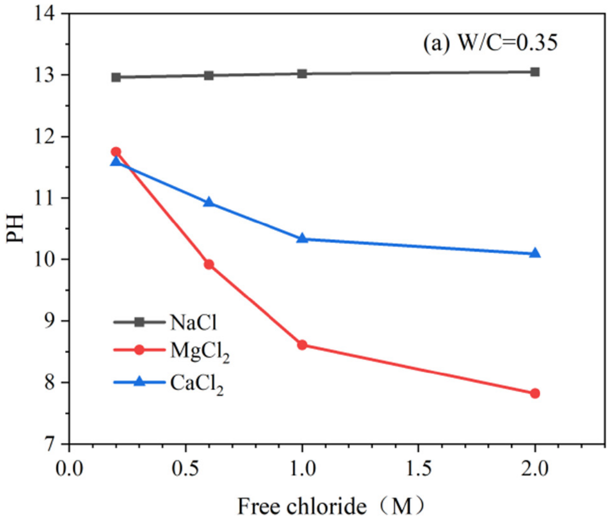

a) W/C = 0.35

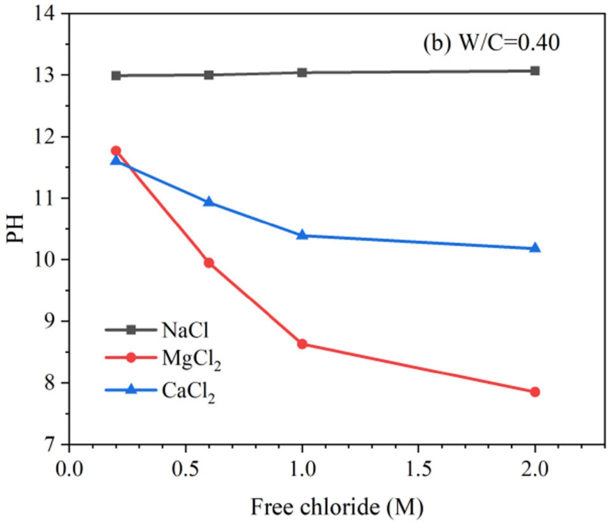

b) W/C = 0.40

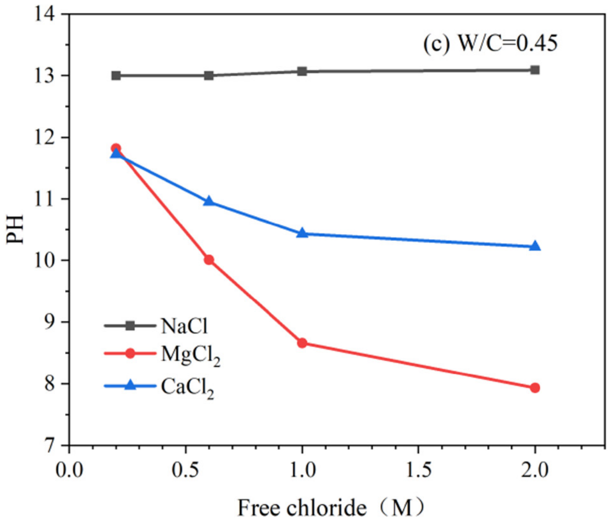

c) W/C = 0.45

Figure 5. The pH value of the supernatant of the exposed solutions.

of Friedel's salt near 11° 2θ with increasing chloride exposure concentrations, indicating promoted Friedel's salt precipitation and consequently the higher chemical chloride binding capacity. Compared to the $CaCl_2$ and $MgCl_2$ systems, the AAS hydration products in the NaCl solutions exhibited generally weaker diffraction peaks. This likely results from the elevated pH of NaCl solutions reducing the solubility of key hydration phases, including Friedel's salt, C-A--S-H, and MgAl-LDHs. This process would release additional bound chloride ions, thereby compromising the chloride-binding capacity of AAS. This explains the relatively lower chloride ion retention observed in AAS exposed to NaCl solutions [26]. Notably, as the concentration of the NaCl exposure solutions increased, the diffraction peak intensity of C-A-S-H (near 29° 2θ) progressively diminished, while the Friedel's salt peak (approximately 11.5° 2θ) intensified. This suggests that C-A-S-H precipitation is partially inhibited in higher-concentration NaCl environments. Concurrently, dissolved Ca^{2+} and Al^{3+} ions from slag preferentially participated in Friedel's salt formation. This predominance is primarily attributed to the abundant chloride ions, which provide both a thermodynamic driving force and additional nucleation sites for Friedel's salt crystallisation. Compared to NaCl solutions, AAS pastes exposed to $MgCl_2$ solutions showed no new hydration products, but exhibited stronger Friedel's salt diffraction peaks, indicating the enhanced chemical binding of chloride ions. Compared to the NaCl and $MgCl_2$ systems, the AAS exposed to $CaCl_2$ solutions exhibited the most pronounced C-A-S-H gel diffraction peak at 29° 2θ. This demonstrates that calcium ions in solution promote C-A-S-H gel formation, thereby enhancing the physical chloride adsorption capacity of AAS [39].

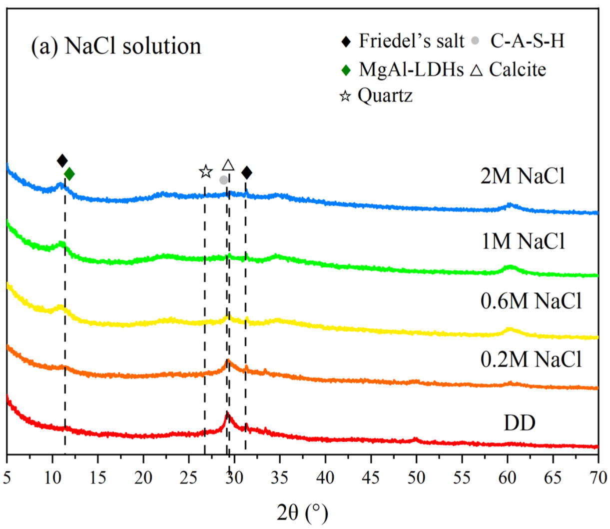

a) NaCl

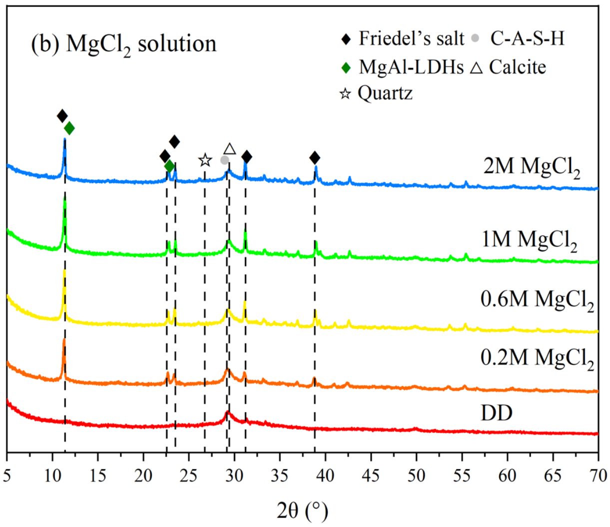

b) $MgCl_2$

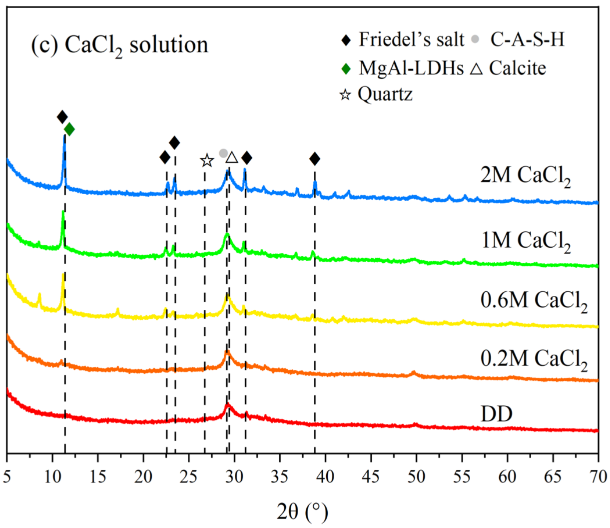

c) $CaCl_2$

Figure 6. XRD patterns of the AAS after exposure to different chloride salt solutions.

TGA analysis

Figure 7 presents the TG-DTG curves of AAS after 28 days of immersion in the chloride solutions. Three distinct peaks are observable in the TG-DTG curves across all three chloride solutions. The first peak, occurring between 30 and 200 °C, is primarily attributed to the thermal decomposition of the interlayer water in C-A-S-H gels [41]. The second peak, observed within the 230 – 410 °C range, corresponds to the mass loss from both the interlayer water in Friedel's salt and the dehydration of the MgAl-LDHs [41]. The broad peak observed between 550 and 650 °C is predominantly associated with carbonate decomposition [38]. The TG-DTG curves reveal more intense peaks near 70 °C for AAS pastes exposed to the $MgCl_2$ and $CaCl_2$ solutions compared to the NaCl systems, indicating greater

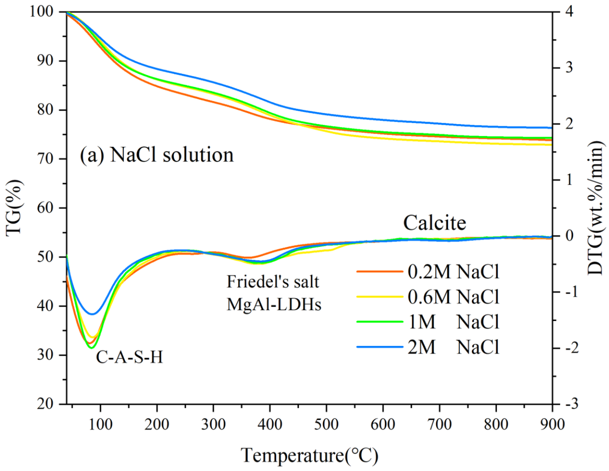

a) NaCl

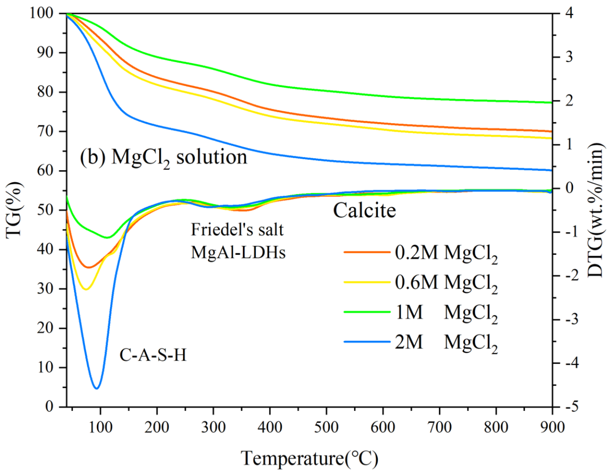

b) $MgCl_2$

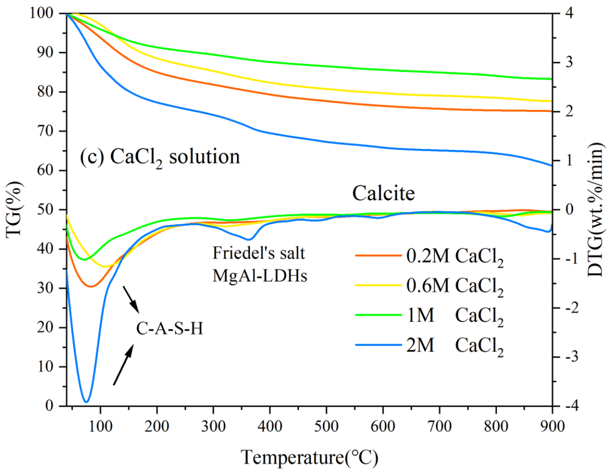

c) $CaCl_2$

Figure 7. The TG-DTG spectra of AAS after exposure to the different chloride salt solutions.

C-A-S-H gel formation in divalent cation environments. This observation aligns with the XRD results and is primarily caused by the elevated pH of NaCl solutions altering the solubility of hydration products. The AAS paste exposed to $CaCl_2$ solution exhibited significantly stronger diffraction peaks (20 % higher intensity) in the 300 – 400 °C range compared to the other two chloride solutions, demonstrating enhanced formation of both Friedel's salt and MgAl-LDHs phases that contribute to the superior chloride binding capacity.

Thermodynamic model analysis

Thermodynamic modelling was employed to predict the stable phase assemblages in AAS following exposure to the different salt solutions. The modelled results for all the groups are presented in Figure 8. Prior to the chloride exposure, the primary hydration products in AAS consisted of C-(N)-A-S-H gel, strätlingite, MgAl-LDH, and trace amounts of natrolite. This finding is consistent with previous thermodynamic modelling results reported in the literature [36]. The formation of Friedel's salt in NaCl-exposed systems confirms the partial chemical binding of chloride ions. Following exposure to the 0.2 and 0.6 M NaCl solutions, the precipitation of Friedel's salt increased progressively with chloride concentration, consistent with experimental observations. Notably, when the solution concentration exceeded 0.6 M, Friedel's salt precipitation reached a plateau, while MgAl-LDHs became destabilised, forming minor brucite. This phenomenon is primarily governed by the aluminium availability in the reaction system. Dissolved Al^{3+} from the slag preferentially reacts with high-concentration chloride ions in the pore solution to form Friedel's salt, consequently suppressing the MgAl-LDH formation. In the $MgCl_2$ solutions, the precipitation of C-(N)-A-S-H gel decreased progressively with the increasing $MgCl_2$ concentration, accompanied by the gradual transformation into M-S-H. As a non-binding phase, M-S-H contributes negligible cohesion to the matrix. This transformation process leads to a significant reduction in the concrete strength [42]. At the 2M concentration threshold, brucite is predicted to occur. This phenomenon is primarily driven by the reaction of excess Mg^{2+} ions in the solution reaching a critical saturation state, resulting in $Mg(OH)_2$ precipitation. Notably, brucite precipitation was not detected in this study. This discrepancy arises because thermodynamic phase predictions assume full chemical equilibrium, whereas the experimental solid-liquid reactions (1 month duration) had not yet reached equilibrium conditions. Compared to the NaCl systems, the $MgCl_2$-exposed specimens exhibited reduced Friedel's salt precipitation, but significantly greater MgAl-LDH formation. MgAl-LDH, as a voluminous phase, has been demonstrated to bind chloride ions through both physical adsorption via electrostatic attraction and chemical incorporation through interlayer anion exchange [43]. This suggests that the chloride-binding capacity of AAS pastes exposed to $MgCl_2$ solutions is predominantly governed

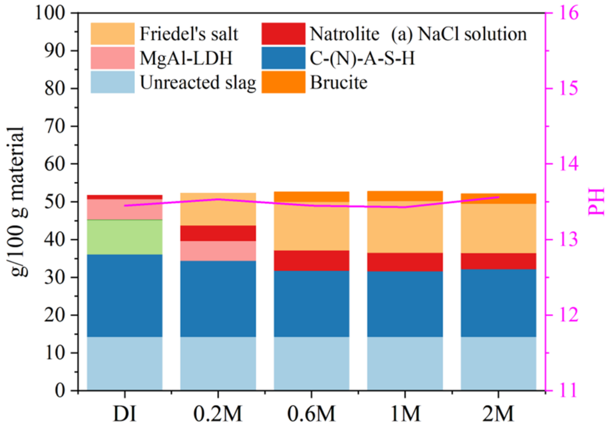

a) NaCl

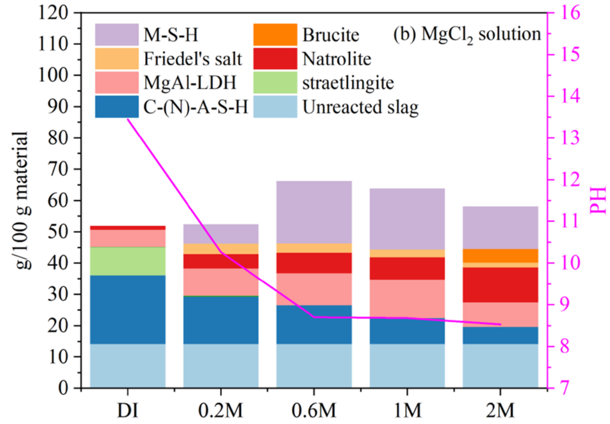

b) $MgCl_2$

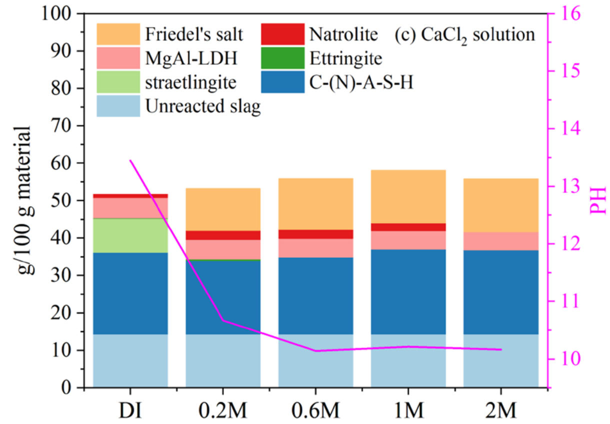

c) $CaCl_2$

Figure 8. The phase combination diagrams of AAS after exposure to the different solutions predicted by the thermodynamic model.

by the MgAl-LDH formation rather than Friedel's salt chemical binding. Compared to the NaCl systems, the $CaCl_2$-exposed AAS exhibited the enhanced formation of both C-A-S-H gel and Friedel's salt, consistent with the experimental observations.

CONCLUSIONS

This study systematically investigates the combined effects of chloride salts on the chloride-binding capacity, phase evolution, and pore solution pH in AAS. Based on the integrated experimental and thermodynamic modelling analyses, the following conclusions can be drawn:

The chloride-binding capacity and pore solution pH of AAS are significantly influenced by the cation types, demonstrating the following binding affinity order: Mg^{2+} > Ca^{2+} > Na^{+}. Compared to the Mg^{2+} and Ca^{2+} systems, the NaCl-exposed AAS maintains higher pore solution pH levels, consequently reducing the solubility of both Friedel's salt and MgAl-LDHs and ultimately diminishing its chloride-binding capacity. AAS exposed to the $MgCl_2$ solution increases the chloride-binding capacity by promoting the precipitation of MgAl-LDHs. The XRD results show that, compared to Mg and Na, Ca is able to generate more C-A-S-H and Friedel's salts, which will respectively contribute to increasing the physical adsorption and chemical binding of the chloride ions in AAS.

Within the water-to-binder (w/b) ratio range of 0.35 – 0.45, increasing the w/b ratio enhances the chloride-binding capacity of AAS, while exerting negligible effects on the pore solution pH.

Compared to the Ca^{2+} and Na^{+} systems, high-concentration Mg^{2+} exerts the most pronounced impact on the pore solution pH levels, primarily attributed to the reactive consumption of hydroxyl groups through the Mg^{2+}-C-A-S-H interactions.

This study reveals the differential effects of different types of chloride salts (NaCl, $MgCl_2$, $CaCl_2$) on the chloride ion binding capacity in alkali-activated slag (AAS). It provides a scientific basis for the application of low-carbon materials in the design of marine engineering and concrete structures in coastal areas, particularly for the optimisation of AAS applications in complex chloride salt environments (such as seawater and de-icing salts). In our future research, we will deepen the investigation into the synergistic effects of chloride salts and other environmental factors (e.g., carbonation, sulfate erosion, freeze-thaw cycles) on the chloride ion binding capacity of AAS. Meanwhile, we will investigate the impact of temperature changes on the stability of chloride ion binding in AAS, particularly the long-term performance in high-temperature and low-temperature environments.

Acknowledgment

We would like to acknowledge the financial support from the International Sci-tech Cooperation Projects under the "Innovation Yongjiang 2035" Key R&D Programme (No. 2024H019).

REFERENCES

1. Da B., Yu H., Ma H., Tan Y., Mi R., Dou X. (2016): Chloride diffusion study of coral concrete in a marine environment. *Construction and Building Materials, 123*, 47-58. doi: 10.1016/j.conbuildmat.2016.06.135
2. Li Y., Chen X., Jin L., Zhang R. (2016): Experimental and numerical study on chloride transmission in cracked concrete. *Construction and Building Materials, 127*, 425-435. doi: 10.1016/j.conbuildmat.2016.10.044
3. Li Q., Ren Z., Su X., Feng Y., et al. (2024): Improving sulfate and chloride resistance in eco-friendly marine concrete: Alkali-activated slag system with mineral admixtures. *Construction and Building Materials, 411,* 134333. doi: 10.1016/j.conbuildmat.2023.134333
4. Xu T., Zhou Z., Wang M., Zhu L., Tian Y., Han D. (2022): Damage mechanism of pier concrete subjected to combined compressive stress, freeze-thaw, and salt attacks in saline soil. *Construction and Building Materials, 324*, 126567. doi: 10.1016/j.conbuildmat.2022.126567
5. Ismail I., Bernal S.A., Provis J.L., San Nicolas R., et al. (2013): Influence of fly ash on the water and chloride permeability of alkali-activated slag mortars and concretes. *Construction and Building Materials, 48*, 1187-1201. doi: 10.1016/j.conbuildmat.2013.07.106
6. Balonis M., Lothenbach B., Le Saout G., Glasser F.P. (2010): Impact of chloride on the mineralogy of hydrated Portland cement systems. *Cement and Concrete Research, 40*(7), 1009-1022. doi: 10.1016/j.cemconres.2010.03.002
7. Liu J., Liu J., Huang Z., Zhu J., Liu W., Zhang W. (2020): Effect of fly ash as cement replacement on chloride diffusion, chloride binding capacity, and micro-properties of concrete in a water soaking environment. *Applied Sciences, 10*(18), 6271. doi: 10.3390/app10186271
8. Chen P., Ma B., Tan H., Liu X. et al. (2020): Effects of amorphous aluminum hydroxide on chloride immobilization in cement-based materials. *Construction and Building Materials, 231*, 117171. doi: 10.1016/j.conbuildmat.2019.117171
9. He H., Qiao H., Sun T., Yang H., He C. (2024): Research progress in mechanisms, influence factors and improvement routes of chloride binding for cement composites. *Journal of Building Engineering, 86*, 108978. doi: 10.1016/j.jobe.2024.108978
10. Chen K.Y., Xia J., Wang S.Q., Wu R.J. et al. (2024): Insights on the chloride adsorption stability in cement mortar under current field and sulfate attack: From experiments to molecular dynamics simulation. *Cement and Concrete Composites, 146*, 105375. doi: 10.1016/j.cemconcomp.2023.105375
11. De Weerdt K., Colombo A., Coppola L., Justnes H., Geiker M.R. (2015): Impact of the associated cation on chloride binding of Portland cement paste. *Cement and Concrete Research, 68*, 196-202. doi: 10.1016/j.cemconres.2014.01.027
12. Qu F., Li W., Guo Y., Zhang S., Zhou J.L., Wang K. (2022): Chloride-binding capacity of cement-GGBFS-nanosilica composites under seawater chloride-rich environment. *Construction and Building Materials, 342*, 127890. doi: 10.1016/j.conbuildmat.2022.127890
13. Chu H., Pan C., Guo M. Z., Cao L., Zhu Z., Song Z., Jiang L. (2020): Influence of cation types on the stability of bound chloride ions in cement mortar simultaneously under electric field and SO_4^{2-} attack. *Construction and Building Materials, 245*, 118402. doi: 10.1016/j.conbuildmat.2020.118402
14. Bakharev T. (2005): Durability of geopolymer materials in sodium and magnesium sulfate solutions. *Cement and concrete research, 35*(6), 1233-1246. doi: 10.1016/j.cemconres.2004.09.002
15. Yang K.H., Song J.K., Song K.I. (2013): Assessment of CO_2 reduction of alkali-activated concrete. *Journal of Cleaner Production, 39*, 265-272. doi: 10.1016/j.jclepro.2012.08.001
16. Yang T., Fan X., Gao X., Gu Q., Xu S., Shui Z. (2022): Modification on the chloride binding capacity of alkali activated slag by applying calcium and aluminium containing phases. *Construction and Building Materials, 358,* 129427. doi: 10.1016/j.conbuildmat.2022.129427
17. Mohebi R., Behfarnia K., Shojaei M. (2015): Abrasion resistance of alkali-activated slag concrete designed by Taguchi method. *Construction and Building Materials, 98*, 792-798. doi: 10.1016/j.conbuildmat.2015.08.128
18. Ismail I., Bernal S.A., Provis J.L., Hamdan S., van Deventer J.S. (2013): Microstructural changes in alkali activated fly ash/slag geopolymers with sulfate exposure. *Materials and Structures, 46*(3), 361-373. doi: 10.1617/s11527-012-9906-2
19. Thomas R.J., Ariyachandra E., Lezama D., Peethamparan S. (2018): Comparison of chloride permeability methods for Alkali-Activated concrete. *Construction and Building Materials, 165*, 104-111. doi: 10.1016/j.conbuildmat.2018.01.016
20. Ye H., Cartwright C., Rajabipour F., Radlińska A. (2017): Understanding the drying shrinkage performance of alkali-activated slag mortars. *Cement and Concrete Composites, 76*, 13-24. doi: 10.1016/j.cemconcomp.2016.11.010
21. Ye H., Radlińska A. (2016): Shrinkage mechanisms of alkali-activated slag. *Cement and Concrete Research, 88*, 126-135. doi: 10.1016/j.cemconres.2016.07.001
22. Duan W., Zhuge Y., Chow C.W., Keegan A., Liu Y., Merta I. (2023): Mitigation of alkali-silica reaction in blast-furnace slag-based alkaline activated material through incorporation of alum water treatment residue. *Construction and Building Materials, 406*, 133383. doi: 10.1016/j.conbuildmat.2023.133383
23. Shi Z., Shi C., Zhang J., Wan S., Zhang Z., Ou Z. (2018): Alkali-silica reaction in waterglass-activated slag mortars incorporating fly ash and metakaolin. *Cement and Concrete Research, 108,* 10-19. doi: 10.1016/j.cemconres.2018.03.002
24. Chen J., Jia J., Zhu M. (2025): Role of supplementary cementitious materials on chloride binding behaviors and corrosion resistance in marine environment. *Construction and Building Materials, 458*, 139724. doi: 10.1016/j.conbuildmat.2024.139724
25. Suryavanshi A.K., Scantlebury J.D., Lyon S.B. (1996): Mechanism of Friedel's salt formation in cements rich in tri-calcium aluminate. *Cement and Concrete Research,*

26(5), 717-727. doi: 10.1016/S0008-8846(96)85009-5

26. Zhu Q., Jiang L., Chen Y., Xu J., Mo L. (2012): Effect of chloride salt type on chloride binding behavior of concrete. *Construction and Building Materials, 37*, 512-517. doi: 10.1016/j.conbuildmat.2012.07.079
27. Pruckner F., Gjørv O.E. (2004): Effect of $CaCl_2$ and NaCl additions on concrete corrosivity. *Cement and Concrete Research, 34*(7), 1209-1217. doi: 10.1016/j.cemconres.2003.12.015
28. Dhir R.K., El-Mohr M.A.K., Dyer T.D. (1996): Chloride binding in GGBS concrete. *Cement and Concrete Research, 26*(12), 1767-1773. doi: 10.1016/S0008-8846(96)00180-9
29. Cai W., Xu Z., Zhang Z., Hu J. et al. (2022): Chloride binding behavior of synthesized reaction products in alkali-activated slag. *Composites Part B: Engineering, 238,* 109919. doi: 10.1016/j.compositesb.2022.109919
30. GB/T 1346-2011 (2011). Test methods for water requirement of normal consistency,setting time and soundness of the Portland cement, China.
31. GB/T 17671-2021 (1999). Method of testing cements-Determination of strength.China Standards Press, China.
32. Luping T., Nilsson L.O. (1993): Chloride binding capacity and binding isotherms of OPC pastes and mortars. *Cement and Concrete Research, 23*(2), 247-253. doi: 10.1016/0008-8846(93)90089-R
33. Ye H., Huang L., Chen Z. (2019): Influence of activator composition on the chloride binding capacity of alkali-activated slag. *Cement and Concrete Composites, 104,* 103368. doi: 10.1016/j.cemconcomp.2019.103368
34. Xu C., Xu D., Zhang W., Ye J., Zhang S. (2024): Influence of steel slag to granulated blast furnace slag ratio on the chloride binding and penetration of metallurgical slag-based binder. *Construction and Building Materials, 431,* 136571. doi: 10.1016/j.conbuildmat.2024.136571
35. Wagner T., Kulik D.A., Hingerl F.F., Dmytrieva S.V. (2012): GEM-Selektor geochemical modeling package: TSolMod library and data interface for multicomponent phase models. *The Canadian Mineralogist, 50*(5), 1173-1195. doi: 10.3749/canmin.50.5.1173
36. Myers R.J., Lothenbach B., Bernal S.A., Provis J.L. (2015): Thermodynamic modelling of alkali-activated slag cements. *Applied Geochemistry, 61*, 233-247. doi: 10.1016/j.apgeochem.2015.06.006
37. Chen K.Y., Miao C., Lyu G.H., Wu K.X., Chen J.J., Xia J. (2025): Developing an indexing methodology for estimating the reactivity of slag from different sources use in alkali-activated materials. *Journal of Non-Crystalline Solids, 647,* 123278. doi: 10.1016/j.jnoncrysol.2024.123278
38. Fu C., Chen Z., Yang G., Ye H. (2024): Synergistic effects of metakaolin and dolomite on alkali-activated slag exposed to chloride and sulfate solutions. *Construction and Building Materials, 420*, 135590. doi: 10.1016/j.conbuildmat.2024.135590
39. Yoshida S., Elakneswaran Y., Nawa T. (2021): Electrostatic properties of C–S–H and CASH for predicting calcium and chloride adsorption. *Cement and Concrete Composites, 121*, 104109. doi: 10.1016/j.cemconcomp.2021.104109
40. Zuo Y., Liu G., Ye J., Gan Y. (2024): Experimental Study and Numerical Modeling of the Solidification Capacity of Chloride Ions in Alkali-Activated Slag Cement Exposed to Sodium Chloride. *ACS Sustainable Chemistry & Engineering, 12*(21), 8104-8114. doi: 10.1021/acssuschemeng.4c00708
41. Wang S.D., Scrivener K.L. (1995): Hydration products of alkali activated slag cement. *Cement and Concrete research, 25*(3), 561-571. doi: 10.1016/0008-8846(95)00045-E
42. Santhanam M., Cohen M.D., Olek J. (2003): Mechanism of sulfate attack: a fresh look: Part 2. Proposed mechanisms. *Cement and Concrete Research, 33*(3), 341-346. doi: 10.1016/S0008-8846(02)00958-4
43. Xu Z., Wu Y., Zhang Z., Wang Y., et al. (2024): Insight into ion exchange behavior of LDHs: Asynchronous chloride adsorption and intercalated ions release processes. *Cement and Concrete Composites, 147*, 105433. doi: 10.1016/j.cemconcomp.2024.105433